

Wideband radar cross section reduction based on absorptive coding metasurface with compound stealth mechanism

Xinmi Yang(杨歆汨), Changrong Liu(刘昌荣), Bo Hou(侯波), and Xiaoyang Zhou(周小阳)
Citation: Chin. Phys. B, 2021, 30 (**10**): 104102. DOI: 10.1088/1674-1056/abf110
Journal homepage: http://cpb.iphy.ac.cn; http://iopscience.iop.org/cpb

What follows is a list of articles you may be interested in

Shared aperture metasurface antenna for electromagnetic vortices generation with different topological charges

He Wang(王贺), Yong-Feng Li(李勇峰), and Shao-Bo Qu(屈绍波)
Chin. Phys. B, 2021, 30 (**8**): 084101. DOI: 10.1088/1674-1056/abe37c

Design of multi-band metasurface antenna array with low RCS performance

Si-Ming Wang(王思铭), Jun Gao(高军), Xiang-Yu Cao(曹祥玉), Yue-Jun Zheng(郑月军), Tong Li(李桐), Jun-Xiang Lan(兰俊祥), Liao-Ri Ji-Di(吉地辽日)
Chin. Phys. B, 2018, 27 (**10**): 104102. DOI: 10.1088/1674-1056/27/10/104102

Ultra-wideband RCS reduction using novel configured chessboard metasurface

Ya-Qiang Zhuang(庄亚强), Guang-Ming Wang(王光明), He-Xiu Xu(许河秀)
Chin. Phys. B, 2017, 26 (**5**): 054101. DOI: 10.1088/1674-1056/26/5/054101

Design of ultra wideband microwave absorber effectual for objects of arbitrary shape

Gong Yuan-Xun, Zhou Zhong-Xiang, Jiang Jian-Tang, Zhao Hong-Jie
Chin. Phys. B, 2015, 24 (**12**): 124101. DOI: 10.1088/1674-1056/24/12/124101

Enhanced absorption property of ordered mesoporous carbon/Co-doped ordered mesoporous carbon double-layer absorber

Guo Shao-Li, Wang Liu-Ding, Wang Yi-Ming, Wu Hong-Jing, Shen Zhong-Yuan
Chin. Phys. B, 2013, 22 (**4**): 044101. DOI: 10.1088/1674-1056/22/4/044101

Wideband radar cross section reduction based on absorptive coding metasurface with compound stealth mechanism*

Xinmi Yang(杨歆汨)[1,2,†], Changrong Liu(刘昌荣)[1], Bo Hou(侯波)[3], and Xiaoyang Zhou(周小阳)[2]

[1] School of Electronics and Information Engineering, Soochow University, Suzhou 215006, China
[2] State Key Laboratory of Millimeter Waves, Nanjing 210096, China
[3] School of Physical Science and Technology & Collaborative Innovation Center of Suzhou Nano Science and Technology, Soochow University, Suzhou 215006, China

(Received 7 January 2021; revised manuscript received 18 March 2021; accepted manuscript online 23 March 2021)

A scheme of combing wave absorption and phase cancellation mechanisms for widening radar cross section (RCS) reduction band is proposed. An absorptive coding metasurface implementing this scheme is derived from traditional circuit analog absorber (CAA) composed of resistive ring elements which characterize dual resonances behavior. It is constructed by replacing some of the CAA elements by another kind of resistive ring elements which is singly resonant in between the original two resonant bands and has reflection phase opposite to that of the original elements at resonance. Hence the developed metasurface achieves an improved low-RCS band over which the lower and higher sub-bands are mainly contributed by wave absorption mainly while the middle sub-band is formed by joint effect of wave absorption and anti-phase cancellation mechanisms. The polarization-independent wideband RCS reduction property of the metasurface is validated by full-wave simulation results of a preliminary and an advanced design examples which employ the same element configuration but different element layout schemes as partitioned distribution and random coding. The advanced design also exhibits broadband bistatic low-RCS property and keeps a stable specular RCS reduction performance with regard to incident elevation angle up to 35°. The advanced design is fabricated and the experimental results of the sample agrees qualitatively well with their simulated counterparts. The measured figure of merit (i.e., low-RCS bandwidth ratio versus electrical thickness) of the sample is 40.572, which is superior to or comparable with those for most of other existing metasurface with compound RCS reduction mechanism. The proposed compound metasurface technique also features simple structure, light weight, low cost and easy fabrication compared with other techniques. This makes it promising in applications such as radar stealth and electromagnetic compatibility.

Keywords: radar cross section (RCS) reduction, coding metasurface, wave absorption, anti-phase cancellation

PACS: 41.20.–q, 41.20.Jb, 84.40.–x **DOI:** 10.1088/1674-1056/abf110

1. Introduction

Radar cross section (RCS) reduction is one of research hotspots in the electromagnetic community. Metasuface is artificial interface that is constructed by spatially arranging customized macroscopic particles in planar or curved surface and that usually has subwavelength thickness. Due to its high degree of freedom in manipulating electromagnetic (EM) waves and easiness in meeting conformal requirements, metasurface has aroused great interest among researchers and become a favorable strategy in exploring novel devices for RCS reduction (RCSR) or EM stealth purpose. To date, most of the metasurfaces developed for RCSR purpose are based on single mechanism, which is mainly wave absorption or scattering pattern regulating. Typical categories of absorptive metasurfaces of concern include circuit analogue absorber (CAA),[1–6] high-impedance surface absorber[7–9] and electromagnetic-matched metamaterial absorber,[10–12] etc. It has been found that the RCSR performance of various absorptive surface with given thickness is constrained by Rozanov limit.[13] Also many scattering pattern regulating schemes have been proposed for RCSR, such as wave-deflection using gradient reflecting-phase,[14–16] grating lobe enhancement,[17,18] anti-phase cancellation,[19–23] polarization-conversion-based destructive interference,[24,25] diffused scattering through random phase distribution or multi-bit coding.[26–29] Another different RCSR mechanism based on hybrid frequency selective surfaces (FSS) was investigated by Genovesi *et al.*[30] Recently, new ideas of mixing wave absorption mechanism with scattering manipulation mechanism for developing low RCS metasurface within wide bandwidth or multi-band has emerged.[31–38] It is expected that the restriction of RCSR performance imposed by either of the two mechanisms alone can be broken through combination of the two mechanisms. In the literature, novel coding metasurface consisting of two kinds of absorptive elements with distinct phase difference was proposed to realize simultaneous control of electromagnetic absorption and phase cancellation.[31,33] In Ref. [32], three different types of lossy scatterers were arranged in single planar array to realize the same mixed RCSR mechanism. Ji *et al.* combined random-phase diffusion and absorption mecha-

*Project supported by the National Natural Science Foundation of China (Grant Nos. 61871280, 61372012, and 61671315).
†Corresponding author. E-mail: yangxinmi@suda.edu.cn
© 2021 Chinese Physical Society and IOP Publishing Ltd

nisms by cascading a geometric-phase metasurface and a resistive frequency selective surface (FSS).[36] Zhuang *et al.* realized a tri-band low-scattering metasurface using combination of diffusion, absorption and regular cancellation.[38] All the instances of metasurface with compound stealth mechanism (compound metasurface for short) listed above exhibit broadband or multi-band low-RCS property with relatively low electrical thickness, but either possess complex structure or require complex fabrication process. In this paper, we propose an alternative scheme of compound metasurface with improved RCSR performance. The proposed compound metasurface is purely composed of simple resistive ring elements and is easy to design and fabricate, while it maintains the wideband feature of RCSR as same as previous works.

The rest of the paper is organized as follows. Section 2 reveals the working principle of the proposed compound metasurface and presents a case of element design for this metasurface. In Section 3, two coding sequence designs of the proposed metasurface are further presented based on the result of element design and the simulation results of the whole compound metasurface designs are given. Section 4 verifies the proposed compound stealth mechanism by measurement results. Finally, a conclusion is drawn in Section 5.

2. Theory and element design

The proposed compound metasurface is inspired by traditional circuit analog absorber (CAA) based on array of resistive square ring elements backed with conducting ground. This kind of CAA has been well studied in Ref. [9]. It has been pointed out that the resistive square ring element is equivalent to a shunt circuit branch with series-connected resistor, inductor and capacitor. When the ring element is properly designed to match the capacitive-inductive response of the grounded substrate, the CAA can achieve dual-resonance or even triple-resonance behavior, which contributes to fairly wide absorption band. An instance of the resistive ring element-based wideband CAA is presented here. Figure 1 shows the geometry and marks the physical dimensions of the resistive ring element employed. The resistive ring is attached on a thin FR-4 substrate, and an air spacer is sandwiched between the substrate and the conducting ground. The thickness, relative permittivity and loss tangent of the substrate are t=0.2 mm, $D_k = 4.4$ and $D_f = 0.02$, respectively. The periodicity of element arrangement is $a_x = a_x = 10$ mm, the thicknesses of the air spacer is $h = 6$ mm. The dimensions (side length d and width w) and the square resistance R_s of the resistive square ring are listed in the 1st line of Table 1. Figure 2 demonstrates the reflection performance of the CAA instance (dashed line). It can be seen that the absorber resonates at two frequencies, which are about 7.6 GHz and 15.8 GHz, respectively. The −10 dB reflection band is from 6.45 GHz to 17.7 5 GHz with a bandwidth ratio (BWR) of 2.75:1. We remark that the −10 dB reflection bandwidth can hardly be further broadened for this absorber, since the absorption performance in the middle sub-band between the lower and upper resonant frequencies deteriorates if one tries to either decrease the lower resonant frequency or increase the upper resonant frequency. However, Fig. 2 also reveals that the reflection phase of the CAA approximates to ±180° in the middle sub-band. This reminds that if a certain number of another kind of resistive square ring elements resonating (i.e., reflecting wave in phase) in the middle sub-band are introduced into the absorber, a nearly 180° difference of reflection phase between the original and newly introduced resistive ring elements and in turn an additional out-of-phase anti-reflection property can be produced in this sub-band. Even if the lower and upper resonant frequencies of the original ring elements become more distant, the anti-reflection property in the middle sub-band can still be maintained in the presence of the newly introduced resistive ring elements. Hence, incorporating two kinds of resistive ring elements which are properly designed into one surface is promising in breaking the bandwidth limit of traditional single-element-based CAA surface.

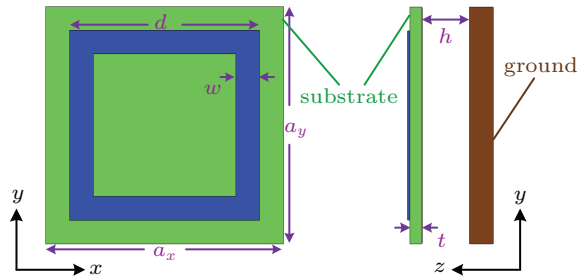


Fig. 1. Front view (left) and side view (right) of resistive ring element involved in the CAA instance and the proposed compound metasurface.

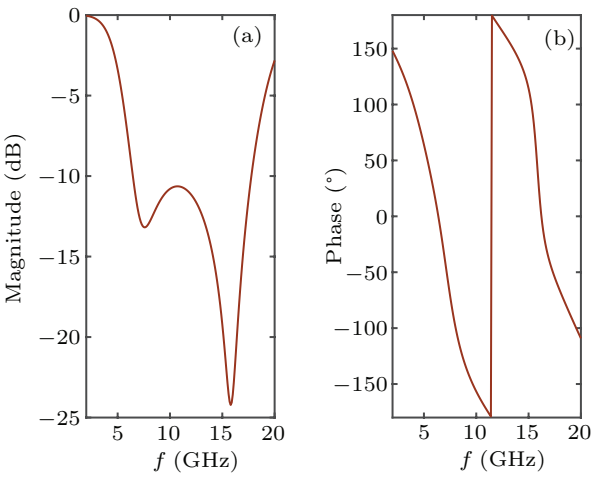


Fig. 2. Reflection magnitude (a) and phase (b) of typical circuit analog absorber composed of resistive ring elements with respect to normally incident TE-polarized plane wave. The curves displayed were obtained from unit-cell simulation in CST microwave studio.

The proposed compound metasurface inspired by the above discussion is a kind of absorptive 1-bit coding metasur-

face composed of two kinds of resistive square ring elements (referred to as element 0 and element 1, respectively, hereinafter) and combines the wave absorption and anti-phase cancellation mechanisms together. The scattering performance of the compound metasurface can be estimated analytically using reflectarray theory.[39] When the metasurface is illuminated by normally incident and TE-polarized (i.e., electric field along the y-axis) plane wave, the scattered far-field intensity in the backward half-space normalized to the peak far-field intensity of a reference conducting plate with the same size as that of the metasurface can be expressed as

$$\bar{I}(\theta,\varphi) = \frac{|S|\sqrt{\sin^2\varphi+\cos^2\theta\cos^2\varphi}}{N_{\mathrm{t}}} \times \left|\sum_{s=0}^{N_y-1}\sum_{l=0}^{N_x-1}\Gamma(l,s)\,\mathrm{e}^{\mathrm{j}k_0\left(ula_x+vsa_y\right)}\right|. \tag{1}$$

The formulation of Eq. (1) has taken both $\hat{\theta}$ and $\hat{\varphi}$ components of scattered field into account. In Eq. (1), $\Gamma(l,s)$ is the local reflection coefficient of resistive ring element labeled by integer pair (l, s) ($l = 0, 1, 2, \ldots, N_x-1$, $s = 0, 1, 2, \ldots, N_y-1$). Value of $\Gamma(l,s)$ is determined using the following classification expression:

$$\Gamma(l,s) = \begin{cases} \Gamma_0, & \text{for element 0,} \\ \Gamma_1, & \text{for element 1,} \end{cases} \tag{2}$$

where Γ_0 and Γ_1 are complex reflection coefficients of resistive ring elements of bit 0 and 1, respectively; they can be obtained from full-wave unit cell simulation assuming periodic boundaries around a single element. Other quantities in Eq. (1) are explained as follows: k_0 is wave number in free space; N_x and N_y are element numbers along the x and y directions, respectively; $N_{\mathrm{t}} = N_x \cdot N_y$ is total element number; u and v are variables related to spherical coordinates or variable observation angles θ and φ by $u = \sin\theta\cos\varphi$ and $v = \sin\theta\sin\varphi$; and S is expressed as

$$S = \mathrm{Sa}\left(\frac{k_0 u a_x}{2}\right)\cdot\mathrm{Sa}\left(\frac{k_0 v a_y}{2}\right), \tag{3}$$

where Sa refers to the sample function.

The effectiveness of the proposed compound metasurface is demonstrated in the rest of this paper through an example operating in a band approximately from 4 GHz to 18 GHz. This example can be viewed as an alteration of the above CAA instance. The basic configurations of the example, including parameters of dielectric substrate, thickness of air spacer and periodicity of ring element, remain unchanged compared with those of the CAA instance. Design of the example consists of two stages: element design and coding sequence design. This section focuses on the element design and the next section deals with the coding sequence design. The element design contains three steps. First, the original resistive ring element in the CAA instance were modified to be element 0. The free parameters (i.e. side length d, width w and square resistance R_{s}) of the original resistive ring element were tuned so that the lower and upper resonant frequencies of these elements shifted to about 5 GHz and 17 GHz, respectively. Second, another kind of resistive ring element named element 1 was introduced and the free parameters was tuned so that it singly resonate at about 9 GHz, where element 0 reflects incident wave with anti-phase. Finally, the free parameters of both kinds of resistive ring element as well as the element ratio $\rho = N_0/N_1$ were optimized to achieve high-level RCSR over the designated wide frequency band. Here N_0 is the number of elements 0. Genetic algorithm capable of dealing with multi-variable problems was applied and a quantity capable of evaluating monostatic RCSR performance over a finite frequency band was employed as the cost function. This quantity is defined by Eq. (4), where f_{l} and f_{u} are the lower and upper bound of the frequency band concerned and $\bar{I}(0,0)$ is the normalized backscattered far field intensity under normal and TE incidence. The expression of $\bar{I}(0,0)$ can be deduced from Eq. (1) and is simplified to

$$F_{\mathrm{cm}} = \max_{f_{\mathrm{l}}\le f\le f_{\mathrm{u}}}\left(\bar{I}(0,0)\right), \tag{4}$$

$$\bar{I}_{\mathrm{m}}(0,0) = \left|\rho\cdot\Gamma_0 + (1-\rho)\cdot\Gamma_1\right|. \tag{5}$$

The optimization process consists of several rounds, each of which takes the six free parameters of the two kinds of resistive ring element as the optimization variables. During each round, the element ratio ρ was assumed as certain fixed number and the six free parameters were optimized through 100 iterations towards the goal of minimizing the cost function F_{cm} within the band from $f_{\mathrm{l}} = 4$ GHz to $f_{\mathrm{u}} = 18$ GHz. The variation ranges of the six free parameters were chosen as the vicinities of the values obtained in the last two steps. The best optimization results were obtained when the element ratio ρ was set as 0.82 and the corresponding optimized values of free parameters are listed in the 2nd and 3rd lines of Table 1.

Table 1. Configurations of resistive ring elements in pure absorptive and compound metasurface designs.

	d	w	R_{s}
Circuit analog absorber	6 mm	0.2 mm	6 Ω
Binary surface (element 0)	7.2 mm	0.6 mm	12.5 Ω
Binary surface (element 1)	5 mm	0.6 mm	373.8 Ω

Figure 3 shows the simulated reflection coefficients of the resistive ring elements 0 and 1 involved in the design example of the compound metasurface. It can be seen that element 0 has two absorption bands which are separated with far distance such that the reflection becomes relatively strong in the middle sub-band between them, while element 1 singly resonates at about 10.7 GHz and has poor absorption performance over the full frequency band. Figure 4 further depicts the reflection phase difference between elements 0 and 1. It is found that in

the middle sub-band which approximately starts from 6 GHz and ends at 15 GHz, the phase difference is within the range of [167.5°, 228.4°]. This offers at least 7.7 dB additional reduction of reflected energy in this band if the energies severally reflected by the areas of elements 0 and 1 are the same. It is remarked that a good achievement of anti-phase cancellation requires nearly equal amounts of reflected energies from the areas of elements 0 and 1. Since the absorption rate of element 0 is much higher than that of element 1 in the middle sub-band, the number of element 0 should be much larger than that of element 1 to ensure a satisfactory anti-phase cancellation performance over this band. This is the reason why a large value of 0.82 was assigned to the element ratio ρ for the presented design. A large ratio of element 0 also ensures that the favorable absorption behavior originated from element 0 is maintained in both the lower and upper sub-bands for the design.

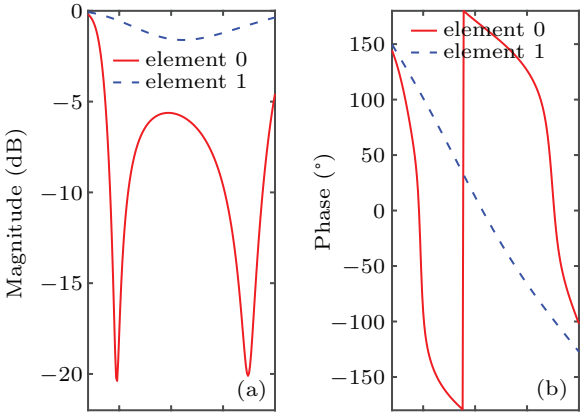


Fig. 3. Reflection magnitude (a) and phase (b) of the resistive ring elements constituting the compound metasurface with respect to normally incident TE-polarized plane wave. The curves displayed were obtained from unit-cell simulation in CST microwave studio.

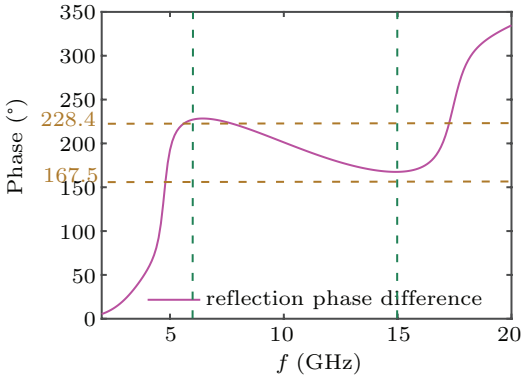


Fig. 4. Simulated reflection phase difference between the resistive ring elements 0 and 1 of the compound metasurface.

The normalized backscattered far-field intensity of the design example under normal incidence was calculated using Eq. (5). Note that the calculated results are irrelevant to the element layout scheme or coding sequence of the design according to Eq. (5). The calculated result is compared with the reflection performance of the aforementioned CAA design in Fig. 5. The 10 dB monostatic RCSR band of the metasurface design is from 4.25 GHz to 18.4 GHz, which is apparently broadened a lot compared with that of the CAA design. The lower and upper sub-bands, which characterize deep valleys in the normalized backscattering curve, are mainly contributed by wave absorption and approximately coincides with the absorption bands of element 0. The middle sub-band results from combined contribution of wave absorption and anti-phase cancellation. In order to gain further physical insight into the stealth mechanism, the ratios of the absorbed energy and the anti-phase cancelled energy (R_a and R_c) in the backscattering direction for the metasurface design were calculated using Eq. (6) and illustrated in Fig. 6. Apparently, one can identify that wave absorption mechanism plays a main role in the lower and higher sub-bands while wave absorption and anti-phase cancellation mechanisms jointly take effect in the middle sub-band.

$$\begin{cases} R_a = \rho \cdot \left(1 - |\Gamma_0|^2\right) + (1-\rho) \cdot \left(1 - |\Gamma_1|^2\right), \\ R_c = 1 - |\rho \cdot \Gamma_0 + (1-\rho) \cdot \Gamma_1|^2 - R_a. \end{cases} \tag{6}$$

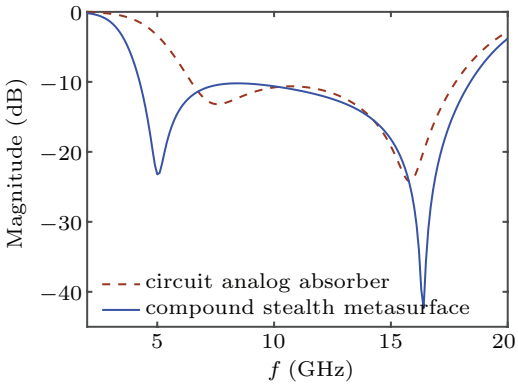


Fig. 5. Comparison of the normalized backscattered far-field intensities of the CAA design and the compound metasurface design under normal incidence. The solid curve was calculated using Eq. (5), while the dashed curve was directly fetched from Fig. 2.

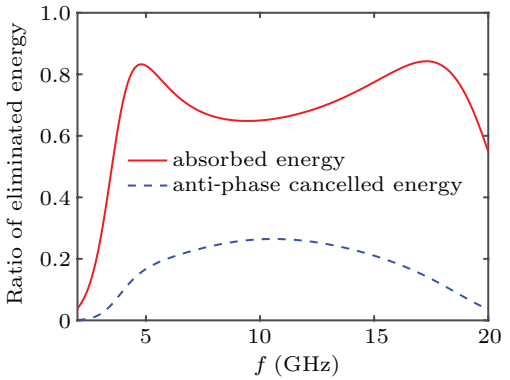


Fig. 6. Ratios of absorbed energy and anti-phase cancelled energy in the backscattering direction for the compound metasurface design under normal incidence. The curves displayed were calculated using Eq. (6).

3. Coding sequence designs and simulation results

Based on the results of element design, a preliminary coding sequence design was exploited and the corresponding element layout is shown in Fig. 7(a). As is shown, the array size of metasurface was set as 22×22 in the design. Hence the relevant element numbers of bit 0 and 1 are $N_0 = 397$ and $N_1 = 87$, respectively. A partitioned distribution scheme was adopted in the preliminary coding sequence design. With this scheme, the whole area of metasurface is divided into two subareas or partitions and elements of bit 0 and 1 are distributed in the two subareas respectively. Such an arrangement is beneficial for lessening the coupling effect between neighboring elements of different kinds. Furthermore, the division of subareas was designed such that the element ratio of $\rho = 0.82$ is approximately maintained in every square annular regions around the metasurface center. This roughly ensures that the ratio of incident wave energies received by areas of elements 0 and 1 keeps stable from the inner to the outer metasurface region when the metasurface is illuminated by horn-emitted wave with a finite beam width in subsequent experiment instead of uniform plane wave assumed in theoretical calculation or simulation.

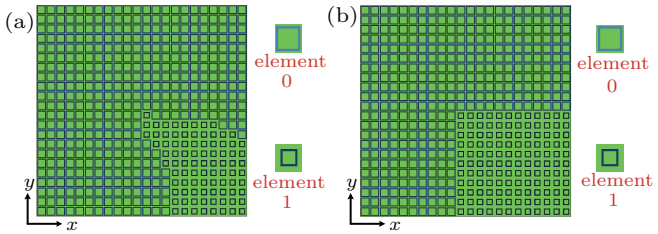


Fig. 7. Element layouts of the (a) preliminary and (b) advanced coding sequence designs for the compound metasurface.

The normalized backscattering performance of the compound metasurface with the preliminary coding sequence design (referred to as the preliminary design for brevity hereinafter) under TE-polarized normal incidence was simulated using CST microwave studio and is compared with its theoretically calculated counterpart in Fig. 8. Overall, the simulated and calculated results have good qualitative agreement but the simulated result shows deteriorated performance in the middle sub-band and the simulated upper absorption band undergoes a violet shift. This discrepancy is mainly due to the ignorance of finite array effect and the coupling between elements 0 and 1 in theoretical calculation. We remark that the simulated RCSR performance of the CAA instance with the same finite scale (22×22) is also worse than its calculated counterparts or the unit-cell simulation results. Also the element layout of the preliminary design is unfavorable for realizing low bistatic RCS. In view of this, an advanced coding sequence design employing random coding scheme was further developed to improve the low RCS performance with regard to both monostatic and bistatic directions.

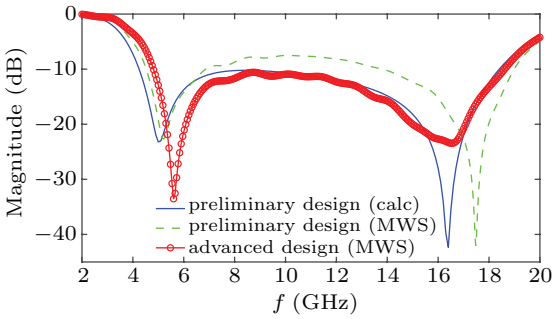


Fig. 8. Normalized backscattered far-field intensities of the preliminary and advanced designs of compound metasurface. The solid curve was calculated from Eq. (1). The dashed and dotted curves were obtained from CST microwave studio.

For the advanced coding sequence design, the whole metasurface area is divided into 11×11 sub-arrays, each of which is composed of 2×2 identical resistive ring elements. Elements of bits 0 and 1 correspond to sub-arrays 0 and 1, respectively. Hence the advanced coding sequence design can be represented by a binary sequence with its length equal to the number of sub-arrays (121). In order to perform an optimization taking both monostatic and bistatic RCS into account, a new cost function $F_{\rm cb}$ was defined. The definition is given by Eq. (7), where w_0 and w_i ($i = 1, 2, 3, \ldots$) are weight coefficients with their sum equal to 1, and $(\theta_{ti}, \varphi_{ti})$ ($i = 1, 2, 3, \ldots$) represent a series of target directions at which bistatic RCS is concerned.

$$F_{\rm cb} = \max_{f_{\rm l} \le f \le f_{\rm u}} \left[w_0 \cdot \bar{I}_{\rm m}(0,0) + \sum_i w_i \cdot \bar{I}_{\rm b}(\theta_{ti}, \varphi_{ti}) \right]. \quad (7)$$

The advanced coding sequence design was obtained through a genetic optimization process, where each individual of population was represented by certain binary sequence of sub-arrays, and the initial population was established through random generation of bits 0 and 1 with the ratio of bit 0 equal to the element ratio obtained in the element design stage ($\rho = 0.82$). The optimization was taken to minimize the cost function $F_{\rm cb}$ within the band from $f_{\rm l} = 4$ GHz to $f_{\rm u} = 18$ GHz with regard to TE-polarized and normally incident plane wave. Scattering at three specific directions, that is, monostatic direction and two bistatic directions of $(\theta_{t1}, \varphi_{t1}) = (9^\circ, 133^\circ)$ and $(\theta_{t2}, \varphi_{t2}) = (6^\circ, 320^\circ)$, were considered in the cost function with weight coefficients w_0, w_1 and w_2 set as 0.4, 0.3 and 0.3, respectively. The element layout related to the advanced coding sequence design is shown in Fig. 7(b). As is shown, the element ratio for the advanced coding sequence design has changed to 0.71. We remark that the advanced coding sequence here is not the best individual with the lowest cost function value in the optimized population. Instead, it is the one with moderate cost function value but high aggregation

degree for both elements 0 and 1. The purpose of such a selection is to lessen the coupling effect between different kinds of elements for the whole metasurface so that the simulated performance will not deviate too much from the theoretical prediction.

The normalized scattered far-field intensities of the compound metasurface with the advanced coding sequence design (referred to as the advanced design for brevity hereinafter) at the aforementioned three specific directions with regard to TE-polarized normal incidence are shown in Fig. 9. Both the results simulated using CST MWS and calculated from Eq. (1) have been presented. Achievement of wideband low RCS property in both monostatic and the two specific bistatic directions is identified from Fig. 9. A roughly qualitative agreement between the simulated and calculated results is observed. The variation trends of the calculated and simulated curves are consistent, although large discrepancy exists between the two sets of curves. Again, the ignorance of finite array effect and the coupling between elements 0 and 1 in theoretical calculation is responsible for this discrepancy. The simulated normalized scattered far-field intensity of the advanced design at monostatic direction is also shown in Fig. 8 to make a comparison with the preliminary design. As is shown, the performance in the middle sub-band has been improved by employing the advanced coding sequence design, with the sacrifice of some shrinkage of −10 dB RCS bandwidth. Figure 10 further depicts the simulated normalized scattering patterns of the advanced design at four sample frequencies. It is confirmed that the scattered energy is diffused so that there is no remarkable scattering lobe above the metasurface with the advanced coding sequence design. The variation of performance of the advanced design with respect to various incident angles and different polarizations was also investigated and is demonstrated in Fig. 11. As is shown, the performance of RCSR is almost insensitive to incident angle for TE polarization as long as the incident elevation angle θ_{I} is below 35°. For TM polarization, although the bandwidth of effective RCSR slowly shrinks as θ_{I} increases, the wideband stealth performance is maintained overall and the 10 dB RCSR bandwidth ratio reaches 1:3 even when θ_{I} is up to 35°.

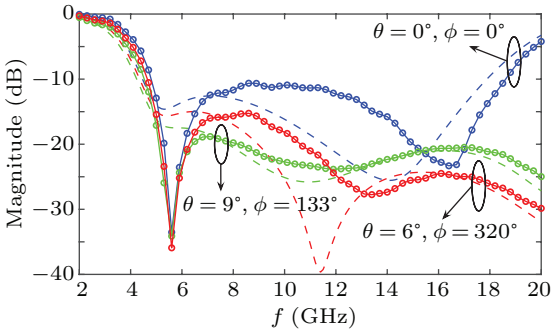


Fig. 9. Normalized monostatic and bistatic scattered far-field intensities of the advanced design. The dashed curves were calculated from Eq. (1) and the solid curves with circle markers were obtained from CST microwave studio.

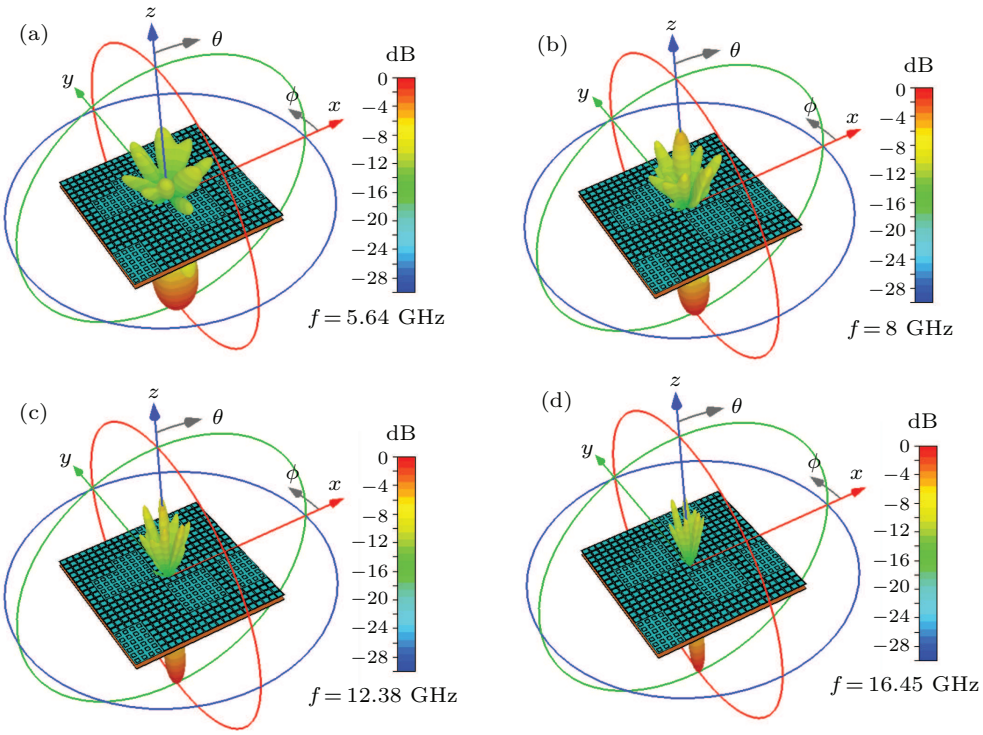


Fig. 10. Simulated scattered far-field patterns of the advanced design normalized to the peak scattered far-field intensity of conducting reference plate with regard to TE-polarized normal incidence at (a) 5.64 GHz, (b) 8 GHz, (c) 12.38 GHz, and (d) 16.45 GHz.

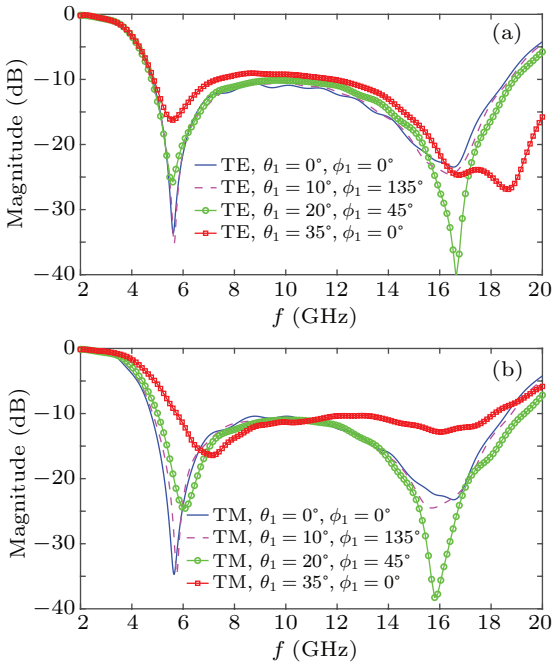


Fig. 11. Normalized intensity of specular far-field scattering of the advanced design with regard to oblique incident angles at (a) TE and (b) TM polarized incidence. The curves displayed were obtained from CST microwave studio.

4. Experimental verification

The compound metasurface with the advanced coding sequence design was fabricated, where the resistive ring array was made from carbon ink using silk-screen printing technique; the FR-4 substrate loaded with the resistive ring array and the metallic ground were fixed together using plastic screws with an air spacer. The fabricated sample is shown in Fig. 12. Experimental verification has been made with regard to the sample. Due to our limited experimental condition, only measurement of specular scattering intensity was conducted. Figure 13 shows the experimental setup for measuring strength of specularly scattered field of the metasurface sample under normal and oblique incidences.

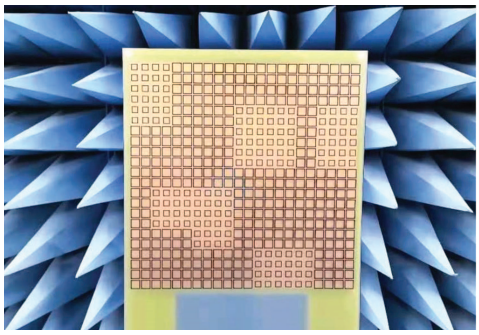


Fig. 12. Front views of compound metasurface sample with the advanced coding sequence design. For this sample, the array of resistive ring elements was printed on a thin FR4 substrate and the substrate was fixed above a metallic plate through plastic screws with an air spacer.

In the setup of normal incidence measurement, a linearly polarized horn antenna is placed along the normal direction of the sample and connected to a vector network analyzer (VNA). During measurement, the horn-VNA combination acts as both a transmitter and a receiver and gated-reflect-line (GRL) calibration technique is applied to eliminate the influence of the wave reflected by the horn itself, so that the reflection coefficient data read from the VNA is only related to the backscattered wave from the sample. The normalized specular scattering intensity of the sample is obtained by normalizing the reflection coefficient data to that acquired when the metasurface sample is replaced by a reference metallic plate of the same size. In the setup of oblique incidence measurement, two linearly polarized horn antennas are placed with mirror symmetry in front of the sample and connected to a signal generator (SG) and a spectrum analyzer (SA), respectively. The spectrum of the specularly reflected field can be detected through synchronized frequency sweeps performed on the SG and the SA. The normalized specular scattering intensity of the sample is obtained by normalizing this spectrum data to that associated with the reference metallic plate.

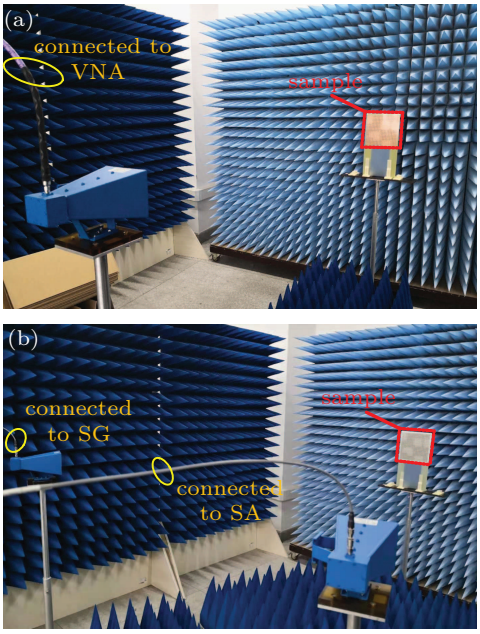


Fig. 13. The experimental setup for measuring strength of specularly scattered field of the compound metasurface sample with (a) normal and (b) oblique incidence.

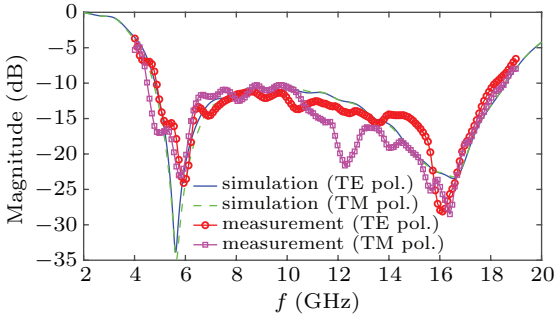


Fig. 14. Comparison of measured and simulated normalized specular scattering intensities of the compound metasurface sample with regard to normal incidence and different polarizations.

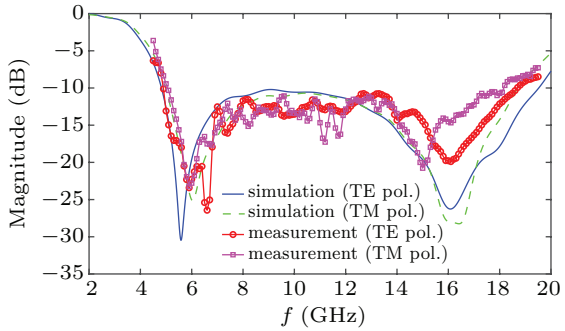


Fig. 15. Comparison of measured and simulated normalized specular scattering intensities of the compound metasurface sample with regard to oblique incidence ($\theta_{\rm I} = 20°$, $\varphi_{\rm I} = 0°$) and different polarizations.

Figure 14 presents the measured curves of normalized specular scattering intensities of the metasurface sample for both TE and TM polarized normal incidences. It is observed that the operation bands of 10 dB reduction of specular reflection or monostatic RCS are from 4.85 GHz to 18.18 GHz, and from 4.51 GHz to 18.54 GHz for TE and TM polarizations, respectively. Figure 15 presents the measured normalized specular scattering intensity of the metasurface sample with regard to oblique incident angle $\theta_{\rm I} = 20°$ and both TE and TM polarizations. It is observed that the specular reflection or bistatic RCS in the band from 4.88 GHz to 18.67 GHz has been reduced by more than 10 dB and 8.3 dB for TE and TM polarizations, respectively. The simulated curves of normalized specular scattering intensities under normal and oblique incidences are also shown in Figs. 13 and 14, respectively, for comparison. The measured results are in good qualitative agreement with their simulated counterparts. The discrepancy between the measured and simulated results is mainly due to the fabrication and assembling error of the sample, the inaccuracy of the experimental setup and material property such as square resistance and substrate permittivity, as well as the effect of finite beam-width of incident wave applied in the experiment.

$$\mathrm{FoM} = \frac{\lambda_{\rm L} \cdot f_{\rm H}}{t_{\rm m} \cdot f_{\rm L}}. \tag{8}$$

In order to better understand the performance of our compound metasurface design, a figure of merit (FoM) has been calculated for the design and compared with those of other reported compound metasurface designs in Table 2. The figure of merit of metasurface for RCSR application is defined by Eq. (8),[37] where $f_{\rm L}$ and $f_{\rm H}$ are the lower and upper ends of 10-dB backscattering reduction (BSR) band with respect to normal incidence, $t_{\rm m}$ is the thickness of metasurface and $\lambda_{\rm L}$ is the free space wavelength at $f_{\rm L}$. For the sake of integrality, the 10-dB BSR bandwidth ratio (BWR $= f_{\rm H}/f_{\rm L}$), the electrical thickness at $f_{\rm L}$ ($t_{\rm me} = t_{\rm m}/\lambda_{\rm L}$), as well as the structure complexity of our design and other designs are also examined in Table 2. Here, the structure complexity is measured by both the number of element types ($N_{\rm e}$) and the number of concrete layers over ground ($N_{\rm l}$) employed by metasurface. All the performance data in Table 2 were evaluated from measurement results. As can be seen from Table 2, the metasurface presented in this work has wider or similar FoM, while possesses a relatively low structure complexity compared with the compound metasurfaces in other works. It should be remarked that our proposed compound metasuface can be easily fabricated using screen printing process and from cheap raw materials (i.e., resistive ink and thin supporting dielectric). Although the structure complexity of Ref. [34] is the same as our work, it has a 3D form and requires much more complex fabrication process.

Table 2. Comparison between our work and other designs of compound metasurface.

References	$N_{\rm e}$	$N_{\rm l}$	$t_{\rm m}$ (mm)	10 dB BSR band (GHz)	BWR	$t_{\rm me}$	FoM
[26]	2	5	3.625	6.8–19.4	2.853:1	0.082	34.721
[27]	3	2	6.12	3.15–18	5.714:1	0.064	88.925
[28]	2	3	4	6.7–19.6	2.925:1	0.089	32.747
[29]	2	2	4	6.4_21.0	3.281:1	0.085	38.452
[31]	1	4	2.3	13–31.5	2.423:1	0.100	24.312
This work	2	2	6.2	4.68–18.365	3.924:1	0.097	40.572

5. Conclusions

We have demonstrated that an absorptive coding metasurface composed of two kinds of resistive ring elements achieves a greatly improved RCSR bandwidth over traditional circuit analog absorber (CAA) consisting of single kind of resistive ring elements. The wide RCSR band is attributed to wave absorption in lower and higher operating sub-bands and joint effect of wave absorption and anti-phase cancellation mechanisms in middle operating sub-band. The proposed compound mechanism for wideband RCSR is verified by both simulation and measurement results of design examples. Properties of polarization insensitivity and good angular stability have also been identified during verification. Compared with other existing compound RCSR techniques, the proposed metasurface possesses low structure complexity and is easy to fabricate. It provides an economic way to meet requirements of radar stealth and electromagnetic compatibility, etc.

References

[1] Munk B A, Munk P and Pryor J 2007 *IEEE Trans. Antennas Propag.* **55** 186

[2] Kazemzadeh A 2011 *IEEE Trans. Antennas Propag.* **59** 135

[3] Shang Y P, Shen Z X and Xiao S Q 2013 *IEEE Trans. Antennas Propag.* **61** 6022

[4] Deng T W, Li Z W and Chen Z N 2017 *IEEE Trans. Antennas Propag.* **65** 5886

[5] Chen J L, Shang Y P and Liao C 2018 *IEEE Antennas Wireless Propag. Lett.* **17** 591

[6] Cheng Y F, Ding X, Peng L, Feng J and Liao C 2020 *IEEE Trans. Antennas Propag.* **68** 1411

[7] Engheta N *IEEE Antennas Propagation Societ Int. Symp.*, June 16–21, 2002 San Antonio, TX, USA, p. 392

[8] Luukkonen O, Costa F, Simovski C R, Monorchio A and Tretyakov S A 2009 *IEEE Trans. Antennas Propag.* **57** 3119

[9] Costa F, Monorchio A and Manara G 2010 *IEEE Trans. Antennas Propag.* **58** 1551

[10] Landy N I, Sajuyigbe S, Mock J J, Smith D R and Padilla W J 2008 *Phys. Rev. Lett.* **100** 207402

[11] Campbell S D and Ziolkowski R W 2013 *IEEE Trans. Antennas Propag.* **61** 1191

[12] Ye D X, Wang Z Y, Xu K W, Li H, Huangfu J T, Wang Z and Ran L X 2013 *Phys. Rev. Lett.* **111** 187402

[13] Rozanov K N 2000 *IEEE Trans. Antennas Propag.* **48** 1230

[14] Sun S L, He Q, Xiao S Y, Xu Q, Li X and Zhou L 2012 *Nat. Mater.* **11** 426

[15] Li Y F, Zhang J Q, Qu S B, Wang J F, Chen H Y, Xu Z and Zhang A X 2014 *Appl. Phys. Lett.* **104** 221110

[16] Wu C J, Cheng Y Z, Wang W Y, He B and Gong R Z 2015 *Acta Phys. Sin.* **64** 164102 (in Chinese)

[17] Doumanis E, Goussetis G, Papageorgiou G, Fusco V, Cahill R and Linton D 2013 *IEEE Trans. Antennas Propagat.* **61** 232

[18] Davenport C J and Rigelsford J M 2014 *IEEE Trans. Antennas Propagat.* **62** 4518

[19] Paquay M, Iriarte J-C, Ederra I, Gonzalo R and de Maagt P 2007 *IEEE Trans. Antennas Propag.* **55** 3630

[20] Edalati A and Sarabandi K 2014 *IEEE Trans. Antennas Propagat.* **62** 747

[21] Chen W, Balanis C A and Birtcher C R 2015 *IEEE Trans. Antennas Propag.* **63** 2636

[22] Liu X, Gao J, Xu L M, Cao X Y, Zhao Y and Li S J 2017 *IEEE Antennas Wireless Propag. Lett.* **16** 724

[23] Huang C, Ji C, Wu X Y, Son J K and Luo X G. 2018 *IEEE Trans. Antennas Propag.* **66** 1628

[24] Jia Y, Liu Y, Guo Y J, Li K and Gong S X 2016 *IEEE Trans. Antennas Propagat.* **64** 179

[25] Zaker R and Sadeghzadeh A 2019 *IEEE Antennas Wireless Propag. Lett.* **18** 1794

[26] Wang K, Zhao J, Cheng Q, Dong D S and Cui T J 2014 *Sci. Rep.* **4** 5935

[27] Zhao J M, Sima B Y, Jia N, Wang C, Zhu B, Jiang T and Feng Y J 2016 *Opt. Express* **24** 27849

[28] Su J X, Lu Y, Liu J Y, Yang Y Q, Li Z R and Song J M 2018 *IEEE Trans. Antennas Propagat.* **66** 7091

[29] Yan X, Liang L J, Zhang Y T, Ding X and Yao J Q 2015 *Acta Phys. Sin.* **64** 158101 (in Chinese)

[30] Genovesi S, Costa F and Monorchio A 2012 *IEEE Trans. Antennas Propag.* **60** 2327

[31] Zhao J, Zhang C, Cheng Q, Yang J and Cui T J 2018 *Appl. Phys. Lett.* **112** 073504

[32] Li F F, Lou Q, Chen P, Poo Y and Wu R X 2018 *Opt. Express* **26** 34711

[33] Shen Y, Zhang J Q, Sui S, Jia Y X, Pang Y Q, Wang J F, Ma H and Qu S B 2018 *J. Phys. D: Appl. Phys.* **51** 485301

[34] Shen Y, Zhang J Q, Shen L H, Sui S, Pang Y Q, Wang J F, Ma H and Qu S B 2018 *Opt. Express* **26** 28363

[35] Zhuang Y Q, Wang G M, Liang J G and Zhang Q F 2017 *IEEE Antennas Wireless Propag. Lett.* **16** 2606

[36] Ji C, Hung C, Zhang X, Yang J N, Song J K and Luo X G 2019 *Opt. Express* **27** 23368

[37] Zhou L and Shen Z X 2020 *IEEE Antennas Wireless Propag. Lett.* **19** 1201

[38] Zhuang Y Q, Wang G M, Zhang Q F and Zhou C 2018 *IEEE Access* **6** 17306

[39] Huang J and Encinar J A 2007 *Reflectarray Antennas* (Hoboken, New Jersey: John Wiley & Sons, Inc.) pp. 68–72